Dalton Transactions

PAPER

View Article Online
View Journal | View Issue

Open Access Article. Published on 03 November 2015. Downloaded on 8/26/2025 8:18:09 AM.
This article is licensed under a Creative Commons Attribution 3.0 Unported Licence.

Cite this: *Dalton Trans.*, 2016, **45**, 156

Magnetic structures of the low temperature phase of $Mn_3(VO_4)_2$ – towards understanding magnetic ordering between adjacent Kagomé layers

Oliver Clemens,*[a,b] Jochen Rohrer[c] and Gwilherm Nénert†[d]

In this article we report on a detailed analysis of the magnetic structures of the magnetic phases of the low temperature (lt-) phase of $Mn_3(VO_4)_2$ (=$Mn_3V_2O_8$) with a Kagomé staircase structure determined by means of powder neutron diffraction. Two magnetic transitions were found at ~25 K (HT1 phase, *Cmc'a'*) and ~17 K (LT1 phase, *Pmc'a'*), in excellent agreement with previous reports. The LT1 phase is characterized by commensurate magnetic ordering of the magnetic moments on two magnetic sites of the Mn1*a*/*b* (2*a* + 2*d*) and Mn2 (8*i*) ions of the nuclear structure (where for the latter site two different overall orientations of magnetic moments within the *ab*-plane (Mn2*a* and Mn2*b*) can be distinguished. This results in mainly antiferromagnetic interactions between edge-sharing Mn-octahedra within the Kagomé planes. The HT1 phase is characterised by strong spin frustration resulting from the loss of ordering of the magnetic moments of Mn2*a*/*b* ions along the *b*-axis. Both magnetic structures are in agreement with the previously reported ferrimagnetic properties of lt-$Mn_3(VO_4)_2$ and shed light on the magnetic phase diagram of the compound reported previously. The magnetic structures are discussed with respect to superexchange interaction pathways within the Kagomé layers, which appear to be predominantly antiferromagnetic. The magnetic structures of $Mn_3(VO_4)_2$ are different compared to those reported for $Ni_3(VO_4)_2$ and $Co_3(VO_4)_2$ and represent an unique commensurate way out of spin frustration for compounds with strong antiferromagnetic superexchange interactions within the Kagomé layers. Additionally, we derive a superexchange model, which will be called redox-mediated M–M'(d^0)–M superexchange and which can help to understand the exclusively ferromagnetic ordering of adjacent Kagomé layers found only for lt-$Mn_3(VO_4)_2$.

Received 14th August 2015,
Accepted 23rd October 2015

DOI: 10.1039/c5dt03141a

www.rsc.org/dalton

1. Introduction

Manganese orthovanadate $Mn_3(VO_4)_2$ (=$Mn_3V_2O_8$) is known to crystallize in two modifications depending on temperature: an orthorhombic low temperature modification (lt-$Mn_3(VO_4)_2$, space group *Cmce*)[1–4] and a tetragonal high temperature modification (ht-$Mn_3(VO_4)_2$, space group $I\bar{4}2d$).[4–6]

ht-$Mn_3(VO_4)_2$ was only discovered recently, and is stable at temperatures above ~946 °C.[4] Due to the reconstructive nature of the phase transition, the phase can be stabilized at ambient temperatures by quick cooling or partial substitution of Mn^{2+} by the single valent alkali metals Li^+ or Na^+.[4–6] The material was shown to order ferrimagnetically below 55 K, and the ferrimagnetic properties agree well with the magnetic structure determined by means of neutron diffraction.

In contrast, the low temperature phase of $Mn_3(VO_4)_2$ has been known for about 40 years.[3] In 2000, Wang *et al.* showed that lt-$Mn_3(VO_4)_2$ can be prepared as a single crystal from a melt containing MoO_3.[2] Clemens *et al.* recently described a facile route to prepare the material *via* a solid state reaction from MnO and V_2O_5, where special care needs to be taken on the grinding and heating procedure, in order to avoid reaction with oxygen.[4]

The structure of lt-$Mn_3(VO_4)_2$ is isotypic to $Ni_3(VO_4)_2$ and $Co_3(VO_4)_2$ [7–12] and characterized as a layered Kagomé staircase lattice. This structural arrangement is well known for its spin frustration within the triangular like edge sharing coordination of MO_6 octahedra (M = Mn, Co, Ni).

$Ni_3(VO_4)_2$ and $Co_3(VO_4)_2$ were extensively studied for their magnetic properties, with $Ni_3(VO_4)_2$ even showing multiferroic

[a]*Technische Universität Darmstadt, Joint Research Laboratory Nanomaterials, Jovanka-Bontschits-Straße 2, 64287 Darmstadt, Germany.*
E-mail: oliver.clemens@kit.edu; Fax: +49 6151 16 6335
[b]*Karlsruher Institut für Technologie, Institut für Nanotechnologie, Hermann-von-Helmholtz-Platz 1, 76344 Eggenstein-Leopoldshafen, Germany*
[c]*Technische Universität Darmstadt, Institut für Materialwissenschaft, Fachgebiet Materialmodellierung, Jovanka-Bontschits-Straße. 2, 64287 Darmstadt, Germany*
[d]*Institut Laue Langevin, 71 Avenue des Martyrs, 38000 Grenoble, France*
†Present address: PANalytical B. V., Lelyweg 1, 7602 EA, Almelo, The Netherlands.

This journal is © The Royal Society of Chemistry 2016

Open Access Article. Published on 03 November 2015. Downloaded on 8/26/2025 8:18:09 AM.
This article is licensed under a Creative Commons Attribution 3.0 Unported Licence.

properties.[7,13,14] The magnetic properties of lt-$Mn_3(VO_4)_2$ were examined on a single crystal by Morosan *et al. via* direction dependent SQUID magnetization measurements. The material was shown to undergo magnetic ordering below T_{m1} = 21 K (ref. 1) (described as the HT1 phase), and the authors report a second phase transition below $T_{m2} \sim 15$ K (described as the LT1 phase). The remanent ferromagnetic magnetisation was reported to be approximately 1.5μ_B per $Mn_3(VO_4)_2$ unit by Wang *et al.*, which is very low compared to the maximum magnetic moment of ~15μ_B per $Mn_3(VO_4)_2$ (expected for ferromagnetic ordering of high spin Mn^{2+} ions) or of ~5μ_B, expected for antiferromagnetic alignment of the Mn ions on the two crystallographic sites within the *Cmce* space group (Mn1 and Mn2), being the 4*a* (Mn1, also referred to as *crosstie* site) and the 8*e* site (Mn2, also referred to as *spine* site). In this respect, Wang *et al.* assume that "the existence of two different occupancies for the Mn sites in this structure is the origin of the ferrimagnetic behaviour observed below $T_C \sim 20$ K".[2]

In the article of Morosan *et al.*, the authors state that neutron diffraction would be a valuable tool to determine the detailed nature of the different magnetic states found for $Mn_3(VO_4)_2$.[1] In this article, we report on a detailed examination of the structures of the magnetic phases of lt-$Mn_3(VO_4)_2$ by means of a temperature dependent powder neutron diffraction study. We will give a detailed description of the exchange interactions arising between the Mn^{2+} ions within the Kagomé planes, and will show that the determined structures are in excellent agreement with magnetisation measurements reported by Wang *et al.*[2] and Morosan *et al.*[1] Furthermore, the magnetic structure which was found for the LT1 phase represents a unique commensurate way to facilitate mainly antiferromagnetic interactions within a spin frustrated Kagomé staircase lattice. In the last part of the article we will discuss differences in the magnetic structures of $Co_3(VO_4)_2$ and in $Ni_3(VO_4)_2$ between the adjacent Kagomé layers, and we will derive a superexchange model to explain magnetic ordering between the adjacent Kagomé planes for lt-$Mn_3(VO_4)_2$ (which will be called redox-mediated M–M′(d^0)–M superexchange).

2. Experimental

2.1 Sample preparation

For the synthesis of lt-$Mn_3(VO_4)_2$, stoichiometric amounts of MnO (99%, Alfa Aesar) and V_2O_5 (99.6+ %, Aldrich) were milled for 2 h in a planetary ball mill (Fritsch pulverisette 7) at a speed of 440 rpm. The as-received powder was pressed into a pellet and heated to 800 °C for 15 h under dry flowing Ar of purity 4.6.

2.2 Neutron diffraction experiments

Neutron powder diffraction (NPD) data to determine the magnetic structure of lt-$Mn_3(VO_4)_2$ were recorded at the Institute Laue-Langevin (Grenoble, France) in the temperature range between 3 and 40 K on the high intensity powder diffractometer D20. The samples were enclosed in a large thin-walled vanadium cylinder. For recording, the high resolution mode including a radial oscillating collimator was applied and an angular range of $3° \leq 2\theta \leq 150°$ (step width $\Delta 2\theta = 0.1°$) was investigated. The total time for a single measurement was approximately 1.2 min. The wavelength of the measurement was determined using $Na_2Ca_3Al_2F_{14}$ to be 2.40 Å. A detailed description of the diffractometer can be found in ref. 15.

Neutron powder diffraction (NPD) data to determine the nuclear structure of lt-$Mn_3(VO_4)_2$ were recorded at the Institute Laue-Langevin (Grenoble, France) at temperatures of 2 K, 18 K, and 32.2 K on the D2B diffractometer. The wavelength of the measurement was calibrated using $Na_2Ca_3Al_2F_{14}$ to be 1.59 Å. A detailed description of the diffractometer can be found in ref. 16.

2.3 Refinement of the magnetic structure

Analysis of neutron diffraction data recorded on the D20 diffractometer was performed using TOPAS Academic V5 [17,18] in the angular range between 10° and 120° 2θ. Reflection broadening was described by convolution of a VOIGT function with a modified pseudo Voigt function according to Thompson–Cox–Hastings.[19] Full details on the analysis and determination of the magnetic structure will be provided in section 3.1.

2.4 Refinements of the nuclear structure

After determination of the principle magnetic structures, the nuclear structures were analysed again using TOPAS Academic V5 [17,18] in the angular range between 5 and 150° 2θ recorded on the D2B diffractometer. Reflection broadening was described by convolution of a VOIGT function with a modified pseudo Voigt function according to Thompson–Cox–Hastings.[19] Positional parameters were refined for all atoms except for vanadium (for which the scattering length for neutrons is very low). Thermal parameters were refined independently, but the same types of atoms were constrained to the same value. Although the magnetic symmetry was shown to break the nuclear symmetry at lowest temperatures, no indications of peak splitting, misfit of intensity, *etc.* could be found and refinements within nuclear subgroups of *Cmce* did not give a significant improvement of the goodness of fit with insignificant shifts of the atoms from the positions being adopted within the *Cmce* symmetry. Therefore, all the nuclear structural data reported in this article refer to a nuclear symmetry of *Cmce*. At this point it is also worth mentioning that refining both, nuclear and magnetic structures at the same time did not result in significant changes of the magnetic moments as found for the data recorded on the D20 diffractometer.

2.5 DFT calculations

Density functional theory (DFT) calculations were performed using the real-space implementation of the GPAW code[20] in conjunction with the PBE[21,22] exchange–correlation functional including Hubbard U corrections.[23] The transition metals are represented by projector-augmented wave setups that contain the outer 4s and 3d electrons as valence states. A grid-spacing of 0.18 Å and a Γ-centered 8 × 4 × 6 *k*-point mesh were used.

Open Access Article. Published on 03 November 2015. Downloaded on 8/26/2025 8:18:09 AM.
This article is licensed under a Creative Commons Attribution 3.0 Unported Licence.

With these computational parameters, we estimate the numerical accuracy for energy differences to be below ±5 meV per formula unit (13 atoms) which is well below the mean physical accuracy of state-of-the-art DFT calculations.

Starting from the experimental structures, atomic positions were optimized until forces did not exceed 0.01 eV $Å^{-1}$. Lattice parameters were then varied and the corresponding energy variations are fitted to quadratic forms as to obtain optimal lattice parameters for each system. At the optimal lattice parameters, atomic structures were finally re-optimized. Structure optimizations were performed using spin-paired calculations. For optimized structures, energetics and electronic structures were then evaluated using spin-polarized calculations with a ferromagnetic and an antiferromagnetic order (see section 3.4).

3. Results and discussion

3.1 Determination and characterisation of the magnetic structure of lt-$Mn_3(VO_4)_2$

Neutron diffraction patterns recorded on the D20 diffractometer at various temperatures are depicted in Fig. 1 (40 K → 17 K) and Fig. 2 (18 K → 3 K). For temperatures below 25 K, the $(0\ 2\ 0)_{Cmce}$ reflection increases in intensity due to the arising of magnetic scattering, with the nuclear scattering contribution to this reflection being basically zero ($I_{nuc}/I_{mag} \sim 1\%$; see Fig. 1). Below 17 K, additional reflections which cannot be indexed within the nuclear space group *Cmce* appear, indicating a second magnetic phase transition (see Fig. 2). Those temperatures are in excellent agreement with the ones reported by Morosan *et al.* (T_{m1} = 21 K and T_{m2} = 15 K),[1] and we assign those magnetic phases to be the HT1 (17 K < T < 25 K) and the LT1 phase (17 K < T).[1]

Pawley fits were performed to determine the magnetic *k*-vector. The HT1 phase can be well described using a single phase with symmetry *Cmce*, indicating *k* to be [0 0 0].

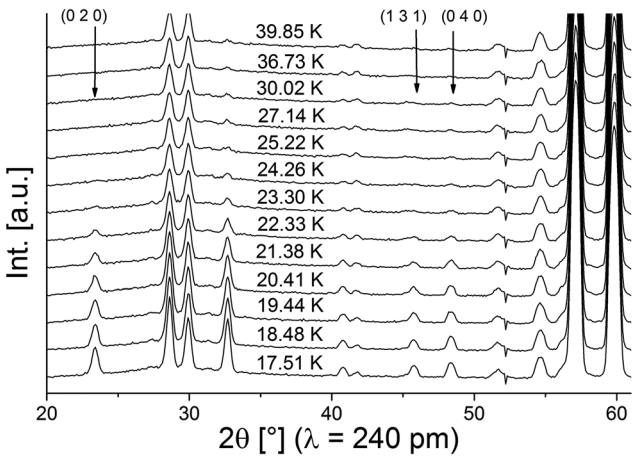

Fig. 1 Neutron diffraction patterns of lt-$Mn_3(VO_4)_2$ in the temperature range between 40 and 17 K. Indexes are given for selected reflections with high magnetic intensity (with *Cmc'a'* being the magnetic symmetry).

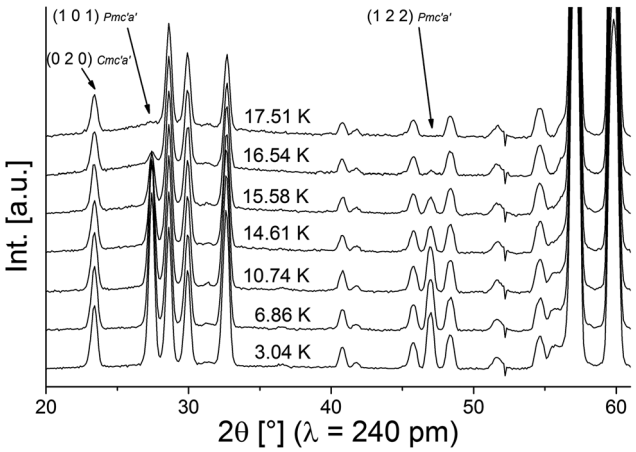

Fig. 2 Neutron diffraction patterns of lt-$Mn_3(VO_4)_2$ in the temperature range between 18 and 3 K. Indexes are given for selected reflections with high magnetic intensity (with *Pmc'a'* being the magnetic symmetry).

For the LT1 phase, it was found that the additional magnetic reflections cannot be described based on k = [0 0 0]. We therefore approached the determination of the magnetic *k*-vector by using Pawley fits with different subgroups of *Cmce*. Doing so, we observed that loss of C-centering is required (*e.g.* from the observation of the (1 0 1) reflection), *e.g.* the nuclear subgroups *Pbnb* (56) and *Pmna* (53) both can be used to obtain equally good description of the pattern. Loss of C-centering is consistent with a magnetic *k*-vector of [1 0 0].

In the next step, full Rietveld analysis was then performed on the patterns recorded at 3.04 K (for the LT1 phase) and 18.48 K (for the HT1 phase) using the nuclear structural model of lt-$Mn_3(VO_4)_2$ as reported in ref. 4, refining only the lattice parameters but not the structural parameters. A second lt-$Mn_3(VO_4)_2$ phase was added with a reduced symmetry of *P*1 for which only the magnetic scattering was calculated and for which structural and lattice parameters were constrained to the nuclear structural model to ensure the maintenance of the higher nuclear symmetry of *Cmce*. However, this reduced symmetry allows for independent refinement of the magnetic moments of all the 12 Mn ions (Mn1 at 4*a* and Mn2 at 8*e* within *Cmce*) per unit cell. Different starting models for the initial orientation of the magnetic moments were tested and the resulting magnetic structures were analysed using the tools provided on the Bilbao Crystallographic Server.[24–29] The best fit obtained for the two different patterns can be summarized as follows:

HT1 phase. For the HT1 phase, we found the magnetic moments to point mainly along the *a*-axis. All Mn1 ions (4*a*) were found to show basically the same magnetic moment along the *a*-axis of ~+3.6μ_B, and all the Mn2 ions (8*e*) were found to show the same magnetic moment of ~−2.5μ_B pointing towards the opposite direction to the Mn1 ions along the *a*-axis. The principal assignment of magnetic moments to crystallographic Mn sites is depicted in Fig. 4a. The orientation of

 This journal is © The Royal Society of Chemistry 2016

Open Access Article. Published on 03 November 2015. Downloaded on 8/26/2025 8:18:09 AM.
This article is licensed under a Creative Commons Attribution 3.0 Unported Licence.

the magnetic moments can be brought in agreement with the magnetic space group *Cmc'a'* (64.475), which is a maximal magnetic subgroup of *Cmce* with k = [0 0 0]. Further analysis shows that the magnetic moments of Mn2 which have been refined along the *c*-axis are very small (~0.1μ_B) and must be considered to be basically zero since the standard deviation obtained for this value was usually 2–3 times as high as the value itself. Therefore, the magnetic moment along the *c*-axis was fixed to zero for all subsequent refinements using the magnetic space group *Cmc'a'*.

LT1 phase. For the LT1 phase, we found that the magnetic moments of the Mn1 ions (4*a*) were basically the same and pointed along the same direction along the *a*-axis. For the ions located on the Mn2 site (8*e*), one could easily identify two different "types" of ions (from now on referred to as Mn2*a* and Mn2*b*), for which the magnetic moments along the *b*-axis of identical magnitude point towards the opposite direction, and the magnetic moments along the *a*-axis are identical with respect to orientation and magnitude. The Mn2*a*/Mn2*b* alternate within the Mn2 channels of edge sharing MnO_6 octahedra along the *a*-axis. The magnetic moment along the *c*-axis again must be considered to be zero within errors for all ions. A schematic drawing of the magnetic structure of the LT1 phase is shown in Fig. 4b. Further analysis of the magnetic subgroups of *Cmc'a'* with k = [1 0 0] showed that the structure can be well described within the magnetic space group *Pmc'a'* (space group 55.357, see Fig. 3). Since *Pmc'a'* is a direct magnetic subgroup of *Cmc'a'*, this is in agreement with the stepwise transition of the magnetic ordering/moments from the HT1 to the LT1 state (see later in this section). At this point, the reader should be aware that both Mn2*a* and Mn2*b* belong to the Wyckoff site 8*i* within *Pmc'a'*. The differentiation

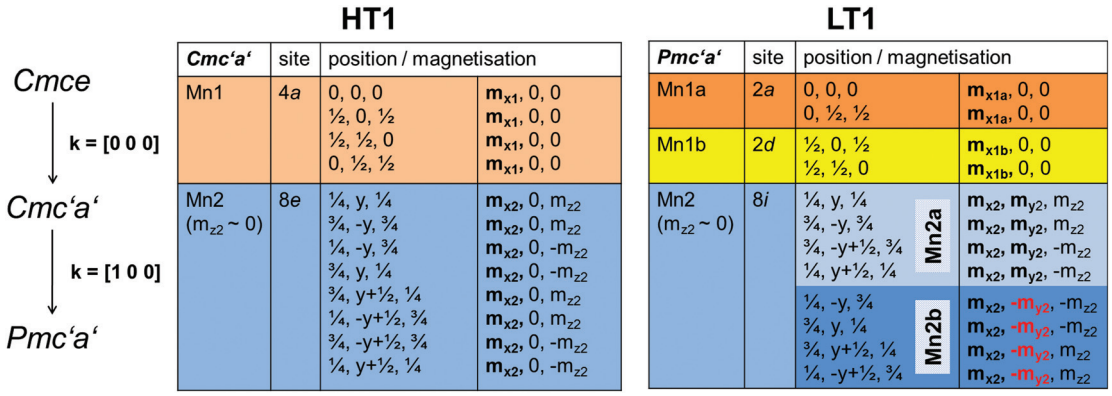

Fig. 3 Symmetry and restrictions for magnetic moments for the transition from the paramagnetic to the HT1 and the LT1 phase of lt-$Mn_3(VO_4)_2$.

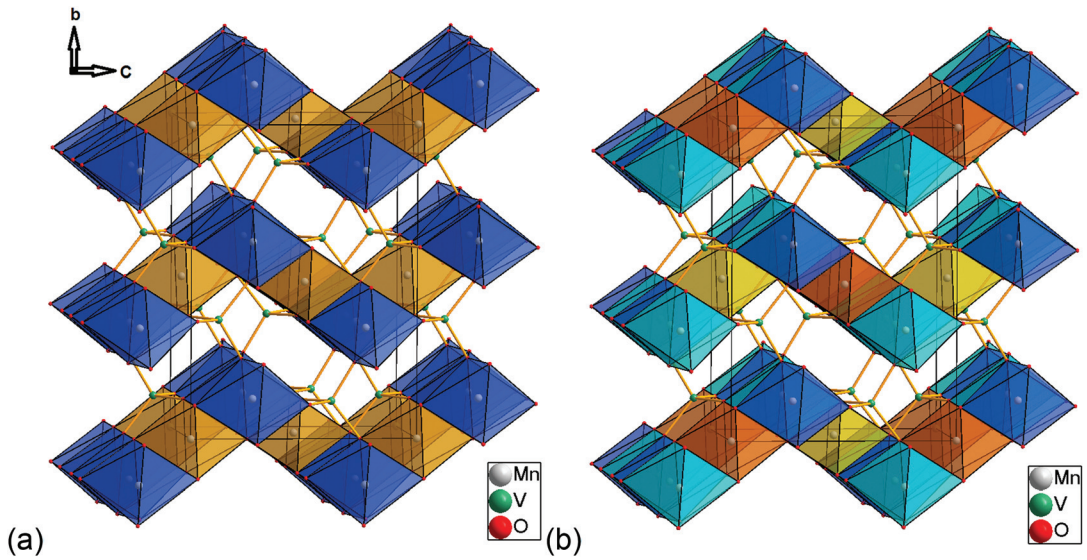

Fig. 4 Scheme of the magnetic structures of the HT1 (a) as well as the LT1 (b) phase of lt-$Mn_3(VO_4)_2$ with view along the *a*-axis (Kagomé planes are stacked along the *b*-axis). (a): Mn1 ions (4*a*) are located in the orange, Mn2 ions (8*e*) are located in the blue octahedra. (b) Mn1*a* ions are located in the dark orange, Mn1*b* ions in the bright orange octahedra. Mn2*a* ions are located in the bright blue, Mn2*b* ions are located in the dark blue octahedra. Moments on atoms with the same colour of the octahedron all point towards the identical direction.

Open Access Article. Published on 03 November 2015. Downloaded on 8/26/2025 8:18:09 AM.
This article is licensed under a Creative Commons Attribution 3.0 Unported Licence.

between those two ions is only made regarding that the magnetic vectors on all Mn2*a* point along the identical direction [m_{x2}, m_{y2}, 0], whereas all the magnetic moments on the Mn2*b* ions point along [m_{x2}, $-m_{y2}$, 0] (*i.e.* Mn2*a* and Mn2*b* do not belong to the same orbit within the space group *Pmc'a'*). This differentiation will however prove useful for the discussion of magnetic properties reported later in this article.

Refined diffraction patterns of lt-$Mn_3(VO_4)_2$ at 3.04 K (LT1), 18.48 K (HT1) and 39.9 K (paramagnetic PM) using magnetic structural models as described above are depicted in Fig. 5. At this point, we would like to point out that we also tried to refine the magnetic scattering using different magnetic space groups (*e.g.* other magnetic subgroups of *Cmce* with $k = [0\ 0\ 0]$) for the measurements at 3.04 and 18.48 K, but such structural models did not result in a proper description of intensities of the magnetic scattering, with R_{wp} values significantly higher according to Hamilton's test.[30]

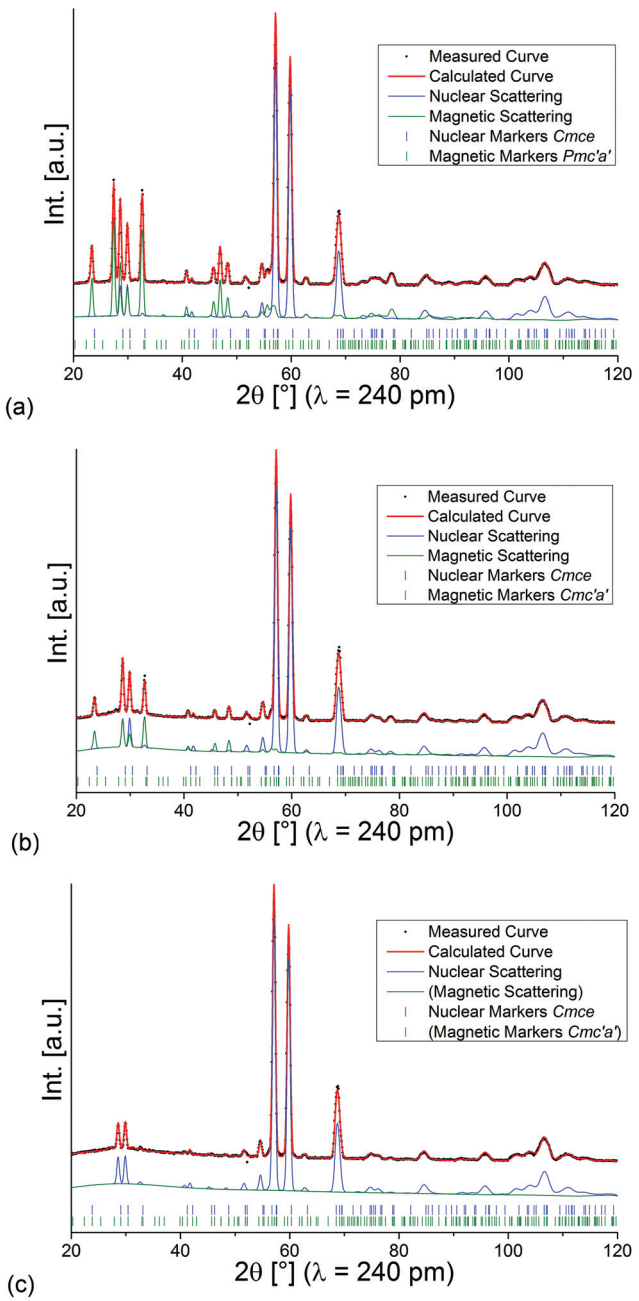

Fig. 5 Rietveld analysis of the neutron diffraction patterns recorded for lt-$Mn_3(VO_4)_2$ at 3.04 K (a), 18.48 K (b), and 39.9 K (c).

We also performed a detailed analysis of the nuclear structures at different temperatures based on the refinement of the higher resolution D2B data. The nuclear structures can be well described within the space group *Cmce* without further lowering of symmetry. Interestingly, it can be seen from the values given in Table 1 that only very subtle structural changes of bond distances and angles can be observed on cooling the compound to temperatures below the magnetic ordering temperatures. Those changes mainly arise from the shift of the O1 and O2 ions, which mainly affects the bond angles ∢(Mn2–O1–Mn2) as well as ∢(Mn2–O2–Mn2), and causes a shrinkage of the bond distance *d*(Mn2–O2) and an increase of the bond distance *d*(Mn2–O1). In addition, the bond distance between Mn1 and Mn2 is found to decrease, whereas the bond distance between Mn2 and Mn2 remains rather constant (*i.e.* the small shift of Mn2 compensates for the decrease of cell volume on cooling for this distance).

3.2 Analysis of magnetic structures in relation to single crystal magnetisation data reported by Morosan *et al.*[1]

Morosan *et al.* already concluded that neutron diffraction would be a valuable tool to relate their observed properties to the magnetic and crystallographic structures.[1] This holds also true the other way around, since the magnetic structures reported here must obviously relate to the magnetic properties of the compounds. Such comparison to the previous studies will be made in the subsequent paragraphs. We will compare the structures reported here to the magnetic measurements at relatively low fields reported by Morosan *et al.*,[1] since our measurements were performed without application of a magnetic field.

The temperature dependence of the magnetic moments on the different Mn ions is shown in Fig. 6. The resulting overall ferrimagnetic moments along the *a*- and the *b*-axes (the axes which were found to show magnetic moments for at least one of the magnetic phases) as well as the resulting total ferrimagnetic moment are depicted in Fig. 7 (the reader should be aware that no net magnetisation is allowed for *Pmc'a'* along the *b*-axis from the site moments given in Fig. 3). A schematic re-drawing of the magnetisation data reported by Morosan *et al.* recorded on a single crystal in different orientations is shown in Fig. 8.

On a first note, a gradual transition from the lower symmetric LT1 phase to the higher symmetric HT1 phase is indicated from the refined moments depicted in Fig. 6. Again, this gradual transition is in agreement with the transition from *Pmc'a'* to *Cmc'a'* being a second order phase transition. The determination of the magnitude of the resulting ferrimagnetic moment along the different crystallographic axes as well as in

Open Access Article. Published on 03 November 2015. Downloaded on 8/26/2025 8:18:09 AM.
This article is licensed under a Creative Commons Attribution 3.0 Unported Licence.

Table 1 Lattice parameters, bond distances and angles of lt-$Mn_3(VO_4)_2$ determined on the D2B diffractometer at temperatures of 2 K, 18 K, 32.2 K, and 100 K. Data determined on a single crystal by Wang *et al.* at ambient temperature are given for comparison.[2] As described in section 2.4, all distances and angles refer to a nuclear symmetry of *Cmce*. Standard deviations are smaller than the digits given

Temperature (Phase)	2 K (LT1)	18 K (HT1)	32.2 K (PM)	100 K (PM)	RT[2] (PM)
∢(Mn1–O3–Mn2) [°]	89.1	89.1	89.0	89.4	89.3
∢(Mn1–O2–Mn2) [°]	90.4	90.5	90.4	90.6	90.2
∢(Mn2–O1–Mn2) [°]	95.9	96.0	95.9	97.1	96.7
∢(Mn2–O2–Mn2) [°]	88.8	88.8	88.9	88.1	88.1
d(Mn1–Mn2) [Å]	3.08	3.08	3.08	3.10	3.09
d(Mn2–Mn2) [Å]	3.12	3.12	3.12	3.13	3.12
d(Mn1–O2) [Å] (×4)	2.11	2.10	2.11	2.10	2.11
d(Mn1–O3) [Å] (×2)	2.21	2.21	2.21	2.22	2.22
$d_{avg.}$(Mn1–O) [Å]	2.14	2.14	2.14	2.14	2.15
d(Mn2–O1) [Å] (×2)	2.10	2.10	2.10	2.09	2.09
d(Mn2–O3) [Å] (×2)	2.18	2.18	2.18	2.18	2.18
d(Mn2–O2) [Å] (×2)	2.23	2.23	2.23	2.25	2.25
$d_{avg.}$(Mn2–O) [Å]	2.17	2.17	2.17	2.17	2.17
a [Å]	6.2343(1)	6.2353(1)	6.2345(1)	6.2596(1)	6.247(1)
b [Å]	11.7162(2)	11.7140(2)	11.7158(2)	11.7296(2)	11.728(2)
c [Å]	8.4874(2)	8.4872(2)	8.4866(2)	8.4969(1)	8.491(2)
$R_{bragg,\ nuc.}$ [%]	1.38	1.37	1.47	1.19	—
$R_{bragg,\ mag.}$ [%]	1.89	2.49	—	—	—

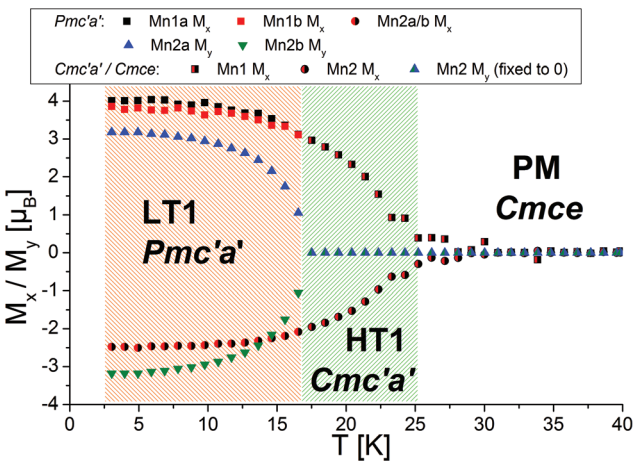

Fig. 6 Temperature dependence of magnetic moments refined for different directions of different atoms within *Pmc'a'* and *Cmc'a'* symmetries. Standard deviations of the refined magnetic moments are in the order of ~0.1–0.2μ_B.

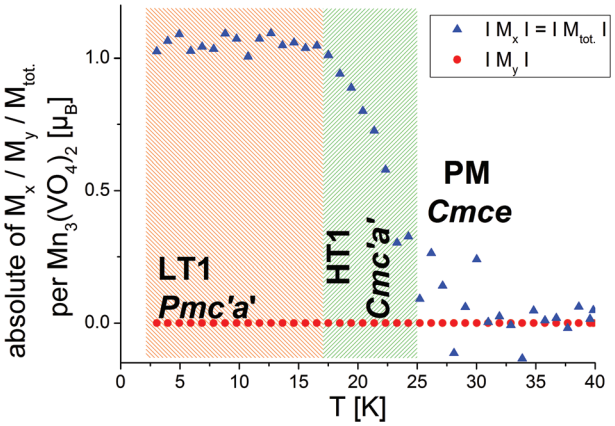

Fig. 7 Ferromagnetic moment per $Mn_3(VO_4)_2$ unit along the *a*- and the *b*-axes as well as in total. The overall magnetisation along the *b*-axis is restricted to be zero from magnetic symmetry for both, the LT1 and the HT1 phase (see Fig. 3).

total indicates an overall ferromagnetic moment of ~1.1μ_B per $Mn_3(VO_4)_2$ unit for the LT1 phase, which is only located along the *a*-axis (see Fig. 7). This value agrees well within errors with the findings of Morosan *et al.*[1] (see Fig. 8) and of Wang *et al.*,[2] where the latter report a ferrimagnetic moment of ~1.5μ_B per $Mn_3(VO_4)_2$ from SQUID measurements of a powdered sample from crushed single crystals.

The magnetic structures also agree well with the measurements reported by Morosan *et al.*,[1] who report that the magnetic easy axis must lie within the *ac*-plane: our findings agree in this respect, showing that the *a*-axis is the magnetically easy axis which carries the main magnetic moment for both the HT1 as well as the LT1 phase, and along which the magnetic moment can be easily flipped. The *c*-axis was shown to carry only a low magnetic moment by Morosan *et al.*[1] This agrees well with our findings which showed that the magnetisation along the *c*-axis must be considered to be close to zero with regards to what can be determined by neutron powder diffraction.

Morosan *et al.*[1] described the *b*-axis as a magnetically hard axis and observed that the temperature dependent behaviour of the magnetisation along this axis is different compared to along the *a*- or the *c*-axis (compare upper figures of Fig. 8): on cooling, the magnetisation along the *b*-axis saturates in the existence range of the HT1 phase, and decreases in the existence range of the LT1 phase down to 2 K (with its absolute value being very small compared to what is found for the *a*-axis). This is in agreement with the strictly overall antiferromagnetic arrangement of the M_y component of the Mn2 ions for the symmetry of the LT1 phase (also see Fig. 3). The loss in magnetic ordering along the

Open Access Article. Published on 03 November 2015. Downloaded on 8/26/2025 8:18:09 AM.
This article is licensed under a Creative Commons Attribution 3.0 Unported Licence.

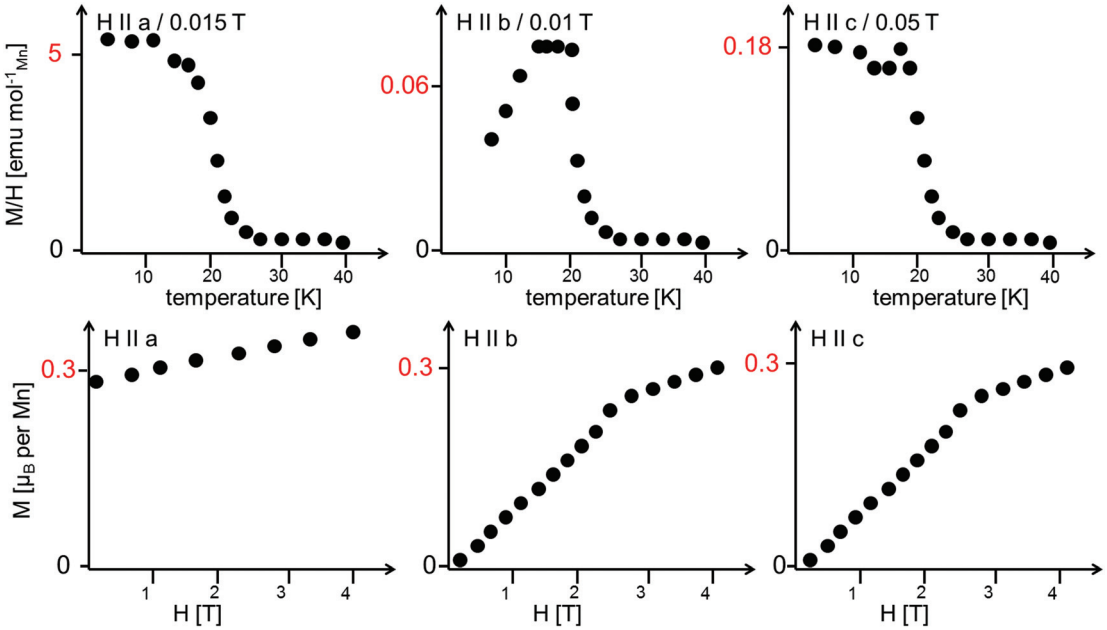

Fig. 8 Schematic re-drawing of the magnetisation data as reported by Morosan *et al.*[1] The reader should note the different scaling for the temperature dependence of the magnetisation. The field-dependent magnetisation curves were recorded at a temperature of 2 K.

b-axis was also found for the phase transition from the LT1 to the HT1 phase of $Ni_3(VO_4)_2$.[14] The orientation of magnetic moments mainly along the *a*-axis is also observed for the incommensurately ordered magnetic compound $Co_3(VO_4)_2$.[31]

Compounds with a Kagomé staircase structure are well known for spin frustration within the Kagomé planes resulting from the triangular coordination situation of edge sharing MO_6 octahedra. It is therefore important to investigate the magnetic structures found for $Mn_3(VO_4)_2$ with respect to the indication of such spin frustration. For the HT1 phase, the magnetic moment of Mn1 was found to be $\sim 3\mu_B$ just above the ordering temperature of the LT1 phase (18.48 K), whereas the overall magnetic moment of Mn2 was refined to be $\sim 2\mu_B$ and therefore significantly smaller. This lowering of the magnetic moment is not the result of *e.g.* a high-spin to low-spin transition, but therefore most likely results from spin frustration on this site. Therefore, in the existence range of the HT1 phase, it is very likely that the individual Mn2 ions carry an additional moment along the *b*-axis. However, this moment must be considered to be randomly oriented, resulting in fluctuating degrees of ferromagnetic and antiferromagnetic interactions along the *b*-axis for the HT1 phase. This existence of magnetic correlations is also well reflected in the appearance of an "amorphous bump" for the HT1 phase (see the isoline plot[32] shown in Fig. 9a). This bump appears at angles where additional magnetic reflections with high intensity are found for the LT1 phase, and therefore indicates that local short range ordering of magnetic moments might still exist. It is therefore reasonable to assume that M_y components of the magnetic moments also exist for the Mn2 ions of the LT1 phase, with orientations m_{y2} and $-m_{y2}$ becoming likely similar. The magnetic transition to the LT1 phase releases spin frustra-

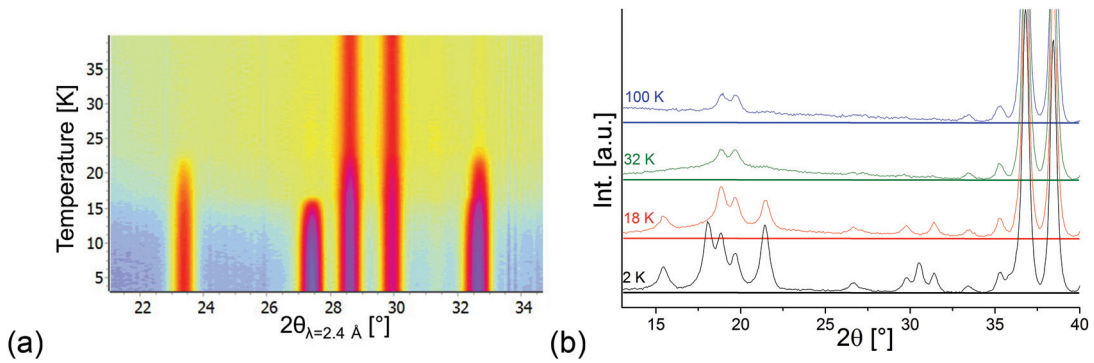

Fig. 9 (a) Isoline plot made using HighScore[32] of D20 data in the temperature range between 3 and 40 K. (b) Behavior of the background for D2B data recorded at different temperatures.

 This journal is © The Royal Society of Chemistry 2016

Open Access Article. Published on 03 November 2015. Downloaded on 8/26/2025 8:18:09 AM. This article is licensed under a Creative Commons Attribution 3.0 Unported Licence.

tion, and the overall magnetic moments on the Mn1a + b as well as Mn2 ions for the LT1 phase become nearly identical and very close to a value of ~4μ_B at 3.04 K (also see Table 2 shown in section 3.3), being in excellent agreement with what was found for ht-$Mn_3(VO_4)_2$ [5] (4.4–3.6μ_B) and Mn^{2+} in a high spin state. This value was also observed for other chemically similar Mn^{2+} compounds, *e.g.* $LiMnPO_4$ [33] (~4.0μ_B). However we recognize that this value can also be found to be significantly higher, *e.g.* ~4.5–5.4μ_B for $MnWO_4$.[34] We therefore conclude that at least most of the spin frustration is released on the magnetic ordering shown by the LT1 phase, although some degree of spin frustration might even be maintained. A further explanation for the deviation from a higher value might be given by the fact that the magnetic moment determined by neutron diffraction is lowered from covalency of bonds to the ligands, and such covalent effects might be different for lt-$Mn_3(VO_4)_2$ (see discussion of redox-induced superexchange interaction reported in section 3.4). Since $L = 0$ for Mn^{2+} must be assumed for Mn^{2+} in a high spin configuration (in agreement with what was found by DFT calculations reported later in this article), a potential orbital contribution to the magnetic moment can be regarded as less plausible.

The "amorphous magnetic bump" persists for temperatures above 25 K (*i.e.* in the paramagnetic state), but disappears when increasing the temperature significantly further (see Fig. 9b). This observation evidences the presence of short range magnetic interactions persisting well above the HT1 phase transition temperature.

$Ni_3(VO_4)_2$ was reported to show a magnetically driven ferroelectric order at lower temperatures.[13] However, the structural analysis reported here suggests that the magnetic phase transitions found for $Mn_3(VO_4)_2$ do not break the spatial inversion symmetry for this compound, ruling out the possibility for multiferroic properties. Both magnetic space groups *Pmc′a′* as well as *Cmc′a′* exhibit the magnetic point group *mm′m′* and thus prohibit the appearance of a linear magnetoelectric effect.[35]

The magnetic structures reported here also show that the transition from the HT1 to the LT1 phase does not result from "the ordering of the spins on one or both of the distinct Mn^{2+} ions in the *ac*-plane" as assumed by Morosan *et al.*,[1] but only originates from the strict antiferromagnetic ordering of the *b*-axis component of the magnetic moment of the Mn2 ions and the release of spin frustration. Overall, the magnetic structures reported here agree well with the magnetisation measurements reported by Wang *et al.*[2] and Morosan *et al.*[1]

3.3 Deriving an understanding of the magnetic structure of the LT1 phase with regards to possible superexchange interactions within the Kagomé plane

Excerpts of the magnetic structures of the LT1 and the HT1 phase are shown in Fig. 10. Since local (but not overall) ordering of moments within the *b*-plane is still likely in the HT1 phase (see discussion before), exchange interaction pathways will be discussed based on the magnetic structural data of the LT1 phase determined at 3.08 K. An overview of relevant bond angles and distances determined by analysis of the D2B data is already given in Table 1, a summary of the magnetic moments found for the different Mn ions for the LT1 as well as for the HT1 phase are given in Tables 2 and 3 respectively.

As already discussed above, the Kagomé staircase structure usually gives rise to spin frustration between edge sharing Mn octahedra within the Kagomé planes due to the triangular interaction situation, and this magnetic frustration is mainly released on a transition from the HT1 to the LT1 phase. To understand the magnetic structure of the LT1 phase of lt-$Mn_3(VO_4)_2$, it is therefore necessary to consider potential magnetic superexchange interactions for edge sharing octahedra between two d^5 high spin cations:[36,37]

1. Direct interactions between d^5 high spin cations result in antiferromagnetic alignment of the magnetic moments.

2. Superexchange promoted *via* an oxygen p-orbital for a 90° bond angle which forms a p_σ bond to one Mn ion and a p_π bond to the other one is antiferromagnetic.

3. Superexchange promoted *via* two different oxygen p-orbitals for a 90° bond angle which form two p_σ bonds to the Mn ions is ferromagnetic and weak (double excitation required).

4. Superexchange promoted *via* an oxygen p-orbital for a bond angle approaching 180°, which forms two p_σ bonds to the Mn ions is antiferromagnetic and very strong. This situation could only be approached for strongly distorted octahedra and must be considered to be of subordinate importance for lt-$Mn_3(VO_4)_2$.

Considering these possible exchange interactions, antiferromagnetic alignment seems to be the most favourable interaction for Mn^{2+} within the Kagomé planes. The angles between the magnetic vectors of the different Mn ions Mn1a/b and Mn2a/b are all larger than 90° (see Tables 2 and 3), which is consistent with such antiferromagnetic interactions. The magnetic structure found for the LT1 phase of lt-$Mn_3(VO_4)_2$ is therefore favourable by facilitating mainly antiferromagnetic interactions between the neighbouring ions according to the superexchange interactions 1 and 2. In particular the angles found between the magnetic vectors of Mn1a/b to Mn2a and Mn2b are relatively high (128°, compare Table 2 to Table 3), highlighting those antiferromagnetic interactions. The angle between the magnetic vectors of Mn2a and Mn2b is lower (104°, again compare Table 2 to Table 3), but still above 90°. Although this interaction should therefore be considered to be of mainly antiferromagnetic nature, it shows the highest ferromagnetic contribution. This could possibly be explained from the subtle changes of the crystallographic structure (reported in Table 1) as follows: the Mn2a–Mn2b distance is larger by about 0.03 Å than for the Mn1a/b–Mn2a/b distance which might result in reduced direct antiferromagnetic interactions between Mn2a and Mn2b. In addition, the Mn1a/b–Mn2/ab distance decreases strongly when cooling down to low temperatures (see Table 1), again facilitating antiferromagnetic exchange between those sites. In addition, the bond angle ∢(Mn2a–O1–Mn2b) decreases by ~1° on cooling, approaching a value of 90°. Such an angle closer to 90° is favourable for the ferromagnetic superexchange interaction (no. 3) between Mn2a and Mn2b. Again this is well supported by the fact that

Open Access Article. Published on 03 November 2015. Downloaded on 8/26/2025 8:18:09 AM.
This article is licensed under a Creative Commons Attribution 3.0 Unported Licence.

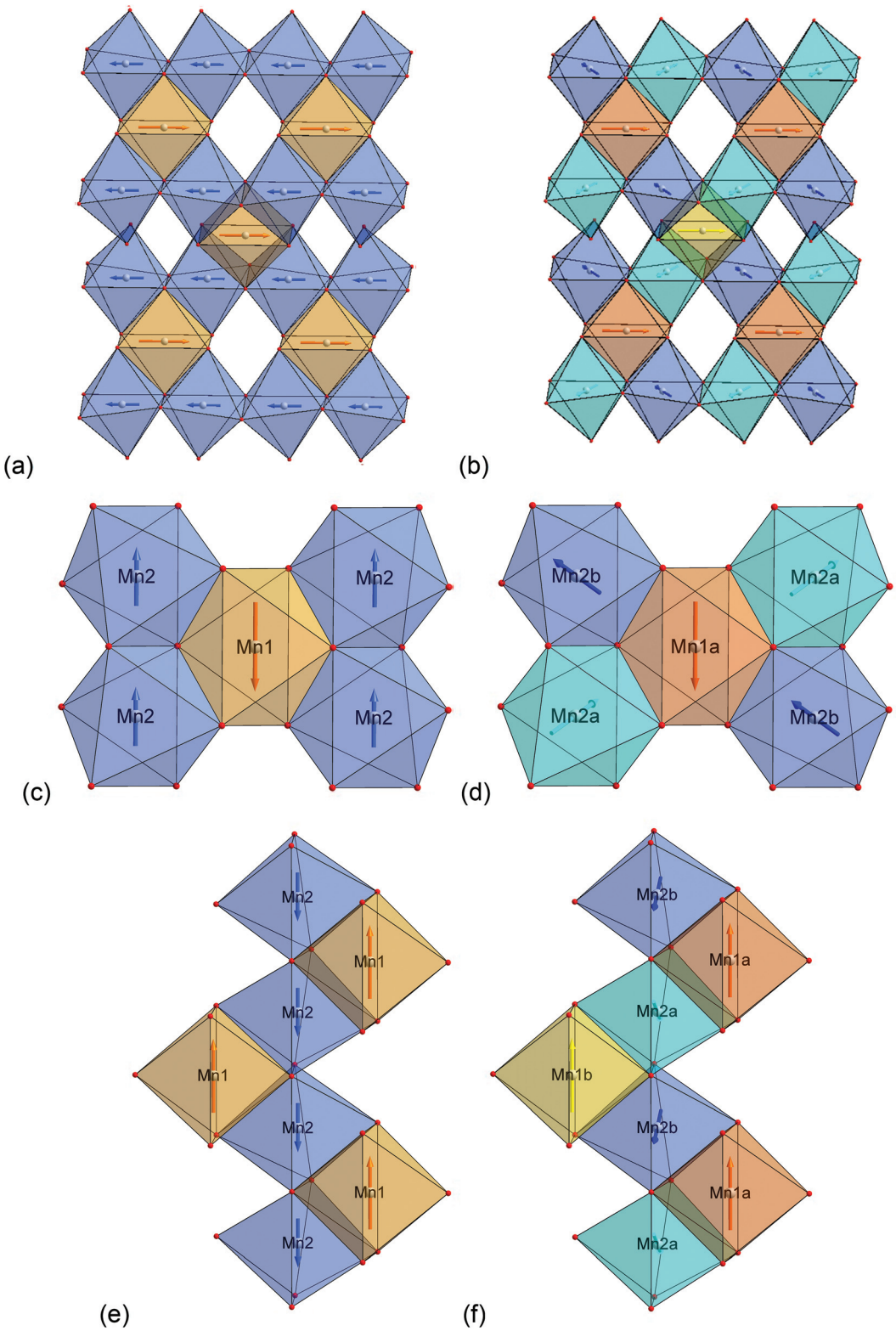

Fig. 10 Structure plots comparing the magnetic structure of the HT1 (a, c, e) with the LT1 (b, d, f) phase of lt-$Mn_3(VO_4)_2$ within one Kagomé staircase plane. Mn1*a* ions are located in the dark orange, Mn1*b* ions in the bright orange octahedra. Mn2*a* ions are located in the bright blue, Mn2*b* ions are located in the dark blue octahedra. (a) and (b) Single Kagomé plane, view slightly tilted along the *b*-axis; (c) and (d) interconnectivity of Mn1 and Mn2 site, viewing direction between the *b*- and *c*-axis; (e) and (f) excerpt of a single spine, view along the *b*-axis.

 This journal is © The Royal Society of Chemistry 2016

Open Access Article. Published on 03 November 2015. Downloaded on 8/26/2025 8:18:09 AM.
This article is licensed under a Creative Commons Attribution 3.0 Unported Licence.

Table 2 Summary of magnetic moments and angles between magnetic vectors found for the LT1 phase of lt-$Mn_3(VO_4)_2$ at 3.04 K

Ion	M_x [μ_B]	M_y [μ_B]	M_z [μ_B]	| M | [μ_B]
Mn1*a*	4.01(13)	0	0	4.0(1)
Mn1*b*	3.86(16)	0	0	3.9(1)
Mn2*a*	−2.48(5)	3.18(4)	0[a]	4.0(1)
Mn2*b*	−2.48(5)	−3.18(4)	0[a]	4.0(1)
Angles between magnetic vectors				
$\sphericalangle(\vec{M}(\mathrm{Mn1}a/b) - \vec{M}(\mathrm{Mn2}a/b))$			128°	
$\sphericalangle(\vec{M}(\mathrm{Mn2}a) - \vec{M}(\mathrm{Mn2}b))$			104°	

[a] The value of $M_{z'}$ was fixed to zero on refinement. As explained before, Mn2*a* and Mn2*b* do not represent two independent crystallographic sites, but only represent two different orientations found for magnetic moments of the Mn2 site

Table 3 Summary of magnetic moments and angles between magnetic vectors found for the HT1 phase of lt-$Mn_3(VO_4)_2$ at 18.08 K

Ion	M_x [μ_B]	M_y [μ_B]	M_z [μ_B]	| M | [μ_B]
Mn1	2.99(6)	0	0	3.0(1)
Mn2	−1.94(5)	0	0[a]	−1.9(1)
Angles between magnetic vectors				
$\sphericalangle(\vec{M}(\mathrm{Mn1}) - \vec{M}(\mathrm{Mn2}))$			180°	
$\sphericalangle(\vec{M}(\mathrm{Mn2}) - \vec{M}(\mathrm{Mn2}))$			0°	

[a] The value of $M_{z'}$ was fixed to zero on refinement.

the alignment of the magnetic moments between those ions shows the lowest antiferromagnetic character (see Tables 2 and 3).

3.4 Comparison of the magnetic structures of the different $M_3(VO_4)_2$ compounds (M = Mn, Co, Ni) – deriving an understanding of magnetic ordering between adjacent Kagomé planes

It is not surprising that superexchange interactions for lt-$Mn_3(VO_4)_2$ ($S = 5/2$, $L = 0$) must be expected to differ in strength and kind from $Co_3(VO_4)_2$ (d^7, $S = 3/2$) and $Ni_3(VO_4)_2$ (d^8, $S = 1$) within the Kagomé planes, where superexchange is promoted *via* direct and indirect superexchange interactions between the interconnected MO_6 octahedra: for $Co_3(VO_4)_2$ ferromagnetic interactions along the channels of edge-sharing Co_2 octahedra were reported by Chen *et al.*,[31] whereas local antiferromagnetic interactions were reported to be dominant along the channels of edge-sharing Ni2 octahedra for the C′ phase (magnetic order stable close to 0 K) of $Ni_3(VO_4)_2$ by Lawes *et al.*.[14] For $Ni_3(VO_4)_2$, the incommensurability along the *a*-axis was also described to arise from the competing antiferromagnetic and ferromagnetic interactions between edge sharing Ni2 octahedra *via* the oxygen ions (direct exchange interactions *via* the double occupied t_{2g} orbitals are non-bonding between two d^8 cations, explained by the varying bond angles for ∢(Ni2–O1–Ni2) and ∢(Ni2–O2–Ni2) from 90.4 to 95° (*i.e.* an angular range which is very sensitive for the competition between both types of interactions).

Remarkably, the different vanadates $M_3(VO_4)_2$ (M = Mn, Co, Ni) also strongly differ with regards to their magnetic ordering between different Kagomé planes along the *b*-axis. For $Mn_3(VO_4)_2$ we found ferromagnetic alignment of the Kagomé planes between the adjacent layers. In contrast, $Ni_3(VO_4)_2$ shows antiferromagnetic alignment of Kagomé planes between the adjacent layers, and $Co_3(VO_4)_2$ shows incommensurate ordering between the Kagomé planes along the *b*-axis, with antiferromagnetic as well as ferromagnetic ordering between the adjacent layers.[31] The Kagomé layers are sort of held together by corner sharing of Mn octahedra with V tetrahedra, with the latter being a cation with d^0 electron configuration and seeming at first glance not to contribute to magnetic interactions. In the following, we will try to derive a microscopic model for orbital interactions in lt-$Mn_3(VO_4)_2$ by developing a new type of superexchange interaction model. This will allow for obtaining a more qualitative, chemically intuitive understanding of the differences of magnetic structures found for the Kagomé staircase compounds $M_3(VO_4)_2$ (M = Mn, Co, Ni) between the adjacent layers.

Apart from the Kagomé staircase compounds, we also note some similarity of the findings reported here to what was observed for $SrM_2(VO_4)_2$ compounds (M = Mn, Co). In the latter, a similar bonding situation with interconnected building blocks of M^{2+} being connected by bridging layers of tetrahedrally coordinated V^{5+} is found.[38] For those two systems similar observations regarding the magnetic structures have been reported by Bera *et al.*,[38] finding a ferromagnetic order *via* the bridging V^{5+} ions for the manganese compound, whereas the cobalt compound was found to show an antiferromagnetic as well as a ferromagnetic order being mediated by V^{5+}.

Electron configurations of the different transition metal cations Mn^{2+}, Co^{2+}, and Ni^{2+} are summarized in Fig. 11. According to Goodenough[36] superexchange between the adjacent Kagomé layers could be promoted *via* M–O–O–M superexchange, *i.e.* cation–anion–anion–cation interactions. For such superexchange interactions, rules for magnetic ordering would be expected to be basically the same as those for M–O–M superexchange interactions and depend on the M–O–O (instead of the M–O–M) bond angles. It must be noted that such superexchange interactions would have to be promoted basically *via* the e_g orbitals of M^{2+} (*i.e.* the d_{z^2} and $d_{x^2-y^2}$ orbitals) which point directly towards the oxide ions. Remarkably, neither the M–O–O bond angles nor the occupations of the e_g orbitals differ significantly for the three transition metal cations Mn^{2+}, Co^{2+}, and Ni^{2+}. From them, mainly antiferromagnetic alignment would have to be expected for all the three compounds (see Fig. 12). Therefore, we think that such M–O–O–M superexchange interactions do not serve well to explain the ferromagnetic arrangement of spins between the adjacent Kagomé layers found for the HT1 phase of $Mn_3(VO_4)_2$ (and also partially for $Co_3(VO_4)_2$).

In this respect, a different type than the M–O–O–M type of superexchange interaction might play a crucial role for $Mn_3(VO_4)_2$ (and to some degree also for $Co_3(VO_4)_2$), which might also be reflected by the fact that ordering between the adjacent Kagomé type layers arises at significantly different temperatures for the three different compounds (see Table 4).

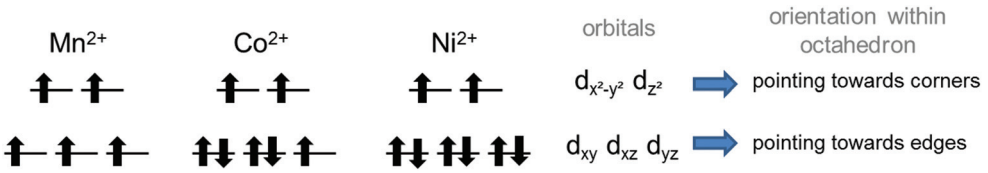

Fig. 11 Electron configurations of the different divalent transition metal ion cations in their high spin states.

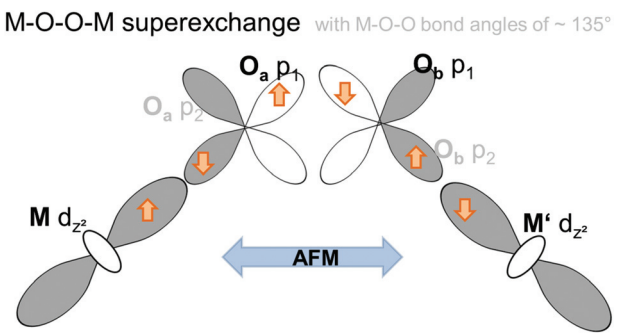

Fig. 12 Schematic presentation of the antiferromagnetic M–O–O–M superexchange interaction promoted *via* half-filled e_g orbitals of two M ions in adjacent Kagomé layers.

Table 4 Temperature below which magnetic ordering between adjacent Kagomé layers starts to occur for different M^{2+} (M = Mn, Co, Ni) and V^{5+} containing compounds

Compound	Temperature below which magnetic ordering between adjacent Kagomé layers starts to occur [K]
$Ni_3(VO_4)_2$	~9.5
$Co_3(VO_4)_2$	8.4
lt-$Mn_3(VO_4)_2$	~25
$SrCo_2(VO_4)_2$ [38]	5.2
$SrMn_2(VO_4)_2$ [38]	42.2

Such a difference is also found for the compounds $SrM_2(VO_4)_2$ (M = Mn, Co).[38] The ordering starts to occur at far higher temperatures for the Mn containing compounds, and is very similar between the Co and Ni containing compounds. It is also worth noting that the magnetic ordering temperature is significantly higher for ht-$Mn_3(VO_4)_2$, for which a 3D-network of interconnected Mn^{2+} coordination polyhedra can be found. Again, this indicates that the type of interaction between the adjacent Kagomé planes can be assumed to differ significantly comparing $Mn_3(VO_4)_2$ with $Co_3(VO_4)_2$ and $Ni_3(VO_4)_2$.

A different superexchange interaction found for Mn^{2+} containing compounds could potentially be promoted by virtual states which involve the empty d-states of the V^{5+} ions (d^0 electron configuration). An influence of the vanadium d-states on the magnetic ordering was suggested by Koo and Whangbo[39] in their study on Ba–Cu–V–O compounds using Extended Hückel Tight Binding (EHTB) calculations, where they considered antiferromagnetic exchange being promoted *via* the V^{5+} ions. Further proof of the involvement of vanadium states was obtained by a ^{51}V NMR study by Ghoshray *et al.* for $BaCu_2(VO_4)_2$,[40] who found a non-zero spin density on the vanadium sites. Ben Yahia *et al.*[41] were also aware of the importance of the vanadium d-levels for magnetic interactions in $KMnVO_4$ (perovskite type compound), for which basically mainly antiferromagnetic interactions have been determined, but one of the four Mn^{2+} remained in a disordered state down to a temperature of 2 K. In the following, we will expand on these considerations using a qualitative structure–chemical approach, and will provide a model of a virtual state for superexchange interactions mediated by V^{5+} which could be used to explain ferromagnetic alignment between the adjacent Kagomé layers found for $Mn_3(VO_4)_2$. We will call this type of interaction redox-mediated M–M′(d^0-)–M superexchange, and give a detailed discussion on how it is facilitated and promoted for the very distinct type of structural arrangement found for lt-$Mn_3(VO_4)_2$. We will also discuss why it should be less expressed for the respective Co and Ni containing compounds. In this respect, the reader will have to be provided with some background knowledge about the chemistry of the different M^{2+} systems with respect to their interaction potentials to V^{5+}.

Clemens *et al.* already observed in an earlier publication that redox instabilities can arise between Mn^{2+} and V^{5+} depending on the initial ratio chosen between MnO and V_2O_5 when trying to prepare $MnO{*}V_2O_5$ compounds.[42] In their case, a reaction with the formation of reaction products according to

$$21Mn^{2+}O + 3V_2{}^{5+}O_5 \rightarrow 4\ Mn^{3+}Mn_4{}^{2+}V^{5+}O_8 + Mn^{2+}V_2{}^{3+}O_4$$

indicates that the redox potentials of Mn^{2+}/Mn^{3+} and V^{3+}/V^{5+} must lie relatively close to each other. In contrast, such redox instabilities are not known to occur between CoO/NiO and V_2O_5,[43] and Fe^{2+} is not stable at all towards V^{5+}.[44] For the latter, this results in the fact that $LiFe^{2+}V^{5+}O_4$ cannot be formed,[44] and no Fe^{2+}/V^{5+} compounds have been reported so far to the best of our knowledge. The redox behaviour of the different divalent M cations is also well reflected *e.g.* in the well-known lithium ion battery cathode materials $LiM^{2+}PO_4$ (M = Fe, Mn, Ni, Co), which show potentials of 3.5 V, 4.1 V, 4.8 V and 5.1 V *vs.* metallic lithium for the oxidation to $M^{3+}PO_4$.[45,46] In a further study, Clemens *et al.* found that doping of $LiMnPO_4$ with vanadium according to $LiMn(PO_4)_{1-x}(VO_4)_x$ (x = 0.1, 0.2) causes an increase of the electrical conductivity of about two orders of

Open Access Article. Published on 03 November 2015. Downloaded on 8/26/2025 8:18:09 AM.
This article is licensed under a Creative Commons Attribution 3.0 Unported Licence.

 This journal is © The Royal Society of Chemistry 2016

Open Access Article. Published on 03 November 2015. Downloaded on 8/26/2025 8:18:09 AM.
This article is licensed under a Creative Commons Attribution 3.0 Unported Licence.

magnitude.[47] This increase of conductivity was explained *via* the partial formation of mixed valence Mn^{2+}/Mn^{3+} by a sort of internal redox process with V^{5+}/V^{4+}, supported by DFT+U based calculations of the partial density of states of such compounds.[47]

Being aware that a sort of internal redox reaction between Mn^{2+} and V^{5+} is indicated from the chemical properties of the transition metal vanadates, DFT calculations were performed to obtain a deeper understanding of relative orbital energies. Two different magnetically ordered states were investigated: an antiferromagnetic and a ferromagnetic interlayer-ordering for all three $M_3(VO_4)_2$ compounds (M = Mn, Co, Ni; see Fig. 13). For the ferromagnetic model, we used a model similar to the HT1 phase of $Mn_3(VO_4)_2$. The antiferromagnetic model is related to the ferromagnetic model in such a way that the Mn1 and Mn2 sites were chosen to order antiferromagnetically within a single Kagomé staircase plane, with assigning antiferromagnetic alignment of the magnetic moments of Mn1 ions in one layer compared to an adjacent layer.

Table 5 summarizes the results obtained for the DFT calculations on the different systems. For Co and Ni, it was found that the AFM ordering seems to be favourable for those compounds, with a small energy difference compared to the FM model. In contrast, we found that for $Mn_3(VO_4)_2$, the ferromagnetic alignment of the layers gives a significant reduction of total energy, well agreeing with the magnetic structure found experimentally. On a further note, lattice parameters reasonably agree with what is observed experimentally.

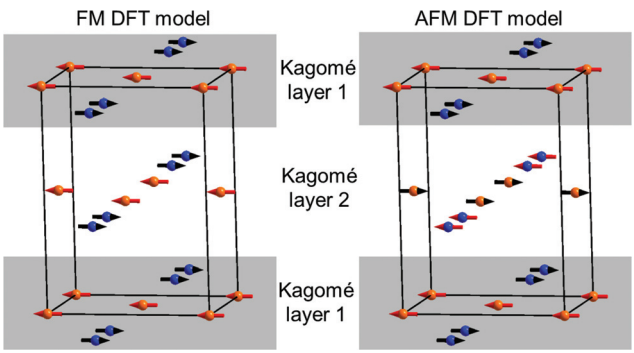

Fig. 13 Substructure of the M ions (M = Mn, Co, Ni) used for spin polarized DFT calculations for the ferromagnetic (FM, left) and the antiferromagnetic (AFM, right) magnetic models. Blue ions refer to the M2 (8*e*) site, orange ions to the M1 (4*a*) site. For the DFT calculations, only overall up (red arrows)/down states (black arrows) were used and no direction of the magnetic vectors are given.

Table 5 Results of DFT+U based calculations of a ferromagnetic and antiferromagnetic model for $M_3(VO_4)_2$ as described in Fig. 13

	Mn	Co	Ni
a [Å]	6.21	6.00	5.98
b [Å]	11.65	11.48	11.49
c [Å]	8.57	8.34	8.23
U [eV] (ref. 48)	3.92	5.05	5.26
E(AFM) − *E*(FM) per $M_3(VO_4)_2$ unit [meV][a]	19.0	−8.8	−2.2

[a] Negative values indicate favouring of the AFM model, positive values indicate favouring of the FM model.

It is a well-known phenomenon that energy corrections for the transition metal d-states need to be applied on such systems.[23,48,49] Indeed, unreasonable densities of states with metallic properties were obtained without compensating for the effects of self-interaction. The energies used for the +U correction are listed in Table 5 and were chosen in relation to chemically similar compounds.[48] Fig. 14 gives an overview about the site projected density states for the M1@4*a* (orange), M2@8*e* (blue) and vanadium ions (green). The density of states calculated using the DFT+U method reasonably agree with a qualitative comparison to the optical properties of the compounds: tetrahedrally coordinated V^{5+} shows usually a white to yellowish colour due to a charge transfer transition from O^{2-} to V^{5+}, well expressed *e.g.* for compounds such as $LiMgVO_4$ and Li_3VO_4.[43,50] For $Co_3(VO_4)_2$, its dark brown colour can be well explained from an interplay of a d–d transition for the Co^{2+} (purple) and a V^{5+}–O^{2-} charge transfer (yellow), the yellowish colour of $Ni_3(VO_4)_2$ is well explained by a d–d transition for Ni^{2+} (yellow) and a V^{5+}–O^{2-} charge transfer (yellow). For $Mn_3(VO_4)_2$, a d–d transition is forbidden from the selection rules, and compounds containing Mn^{2+} are usually found to show a white (*e.g.* $LiMnPO_4$ [43]) colour if other transitions in the visible range of the energy spectrum are not present at the same time. Therefore, the strong red colour found for $Mn_3(VO_4)_2$ [43] would be explained by an additional charge transfer transition from Mn^{2+} to V^{5+}. This is in principle agreement with the fact that such a transition would be allowed regarding the selection rules. Overall, these observations are in principle agreement with the tendency of the band gaps found in our DFT calculations.

The filled d-levels of the M^{2+} ions below the Fermi level approach the empty d-levels of vanadium above the Fermi level when changing from Ni→Co→Mn. This agrees well with the chemical properties of the compounds as discussed in previous paragraphs (*e.g.* oxidation potentials of $LiMPO_4$ compounds). If the V^{5+} levels interact with the Mn^{2+} states to result in a superexchange interaction, it is a well-known principle of any bonding theory that the interacting states must be similar regarding their energy. Again, this phenomenon is well expressed for $Mn_3(VO_4)_2$, where the occupied $d_{x^2-y^2}$ and d_{z^2} states close below the Fermi level are separated by only about 1 eV to the unoccupied d-levels of vanadium above the Fermi level. Additionally, we found that the splitting of the vanadium d-levels in the tetrahedral ligand field is significantly lower compared to the splitting of the d-levels of manganese in the octahedral ligand field, as would be expected.

Apart from the energetic similarity of orbital states, a reasonable orbital interaction pathway must be present to facilitate a superexchange interaction (which would translate to sort of a good overlap integral of the different atoms). There-

Open Access Article. Published on 03 November 2015. Downloaded on 8/26/2025 8:18:09 AM.
This article is licensed under a Creative Commons Attribution 3.0 Unported Licence.

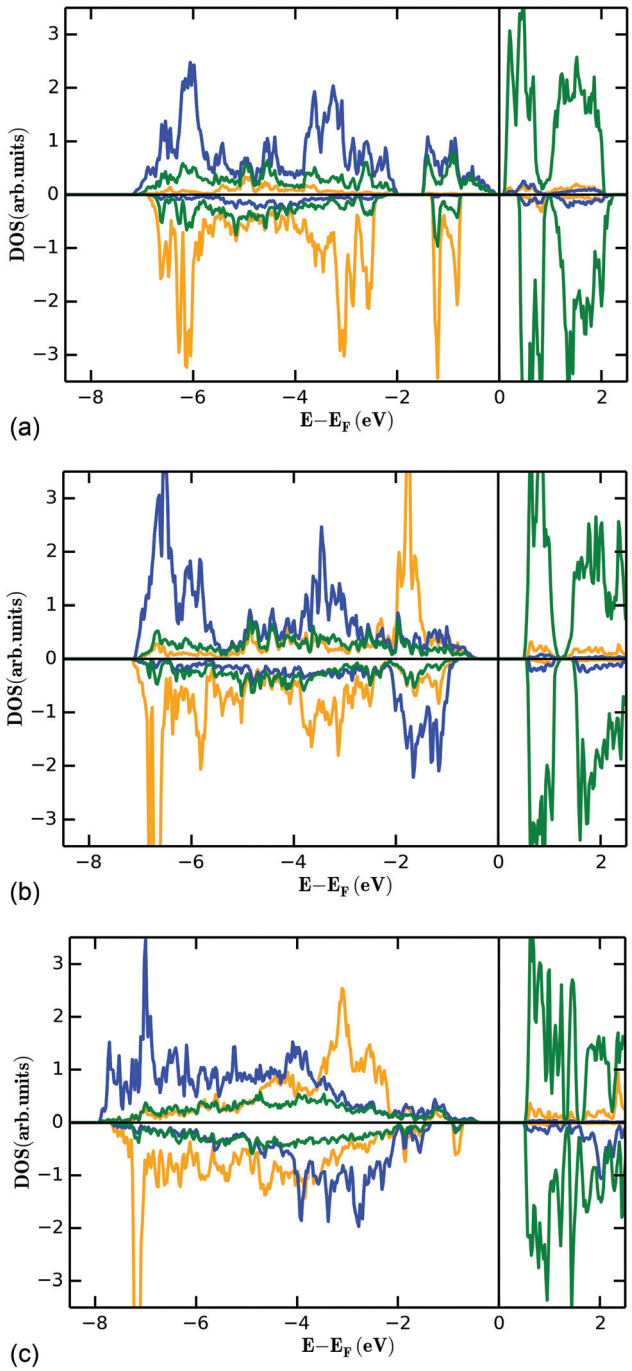

Fig. 14 Partial density of states for the FM state (see Fig. 13) of the M1 (4*a*, orange), M2 (8e, blue) and vanadium (green) ions for $Mn_3(VO_4)_2$ (a), $Co_3(VO_4)_2$ (b), and $Ni_3(VO_4)_2$ (c).

fore, we will now discuss structural pathways with potential orbital overlap along which such ferromagnetic ordering interactions could arise within lt-$Mn_3(VO_4)_2$. The following discussion will help to explain the ferromagnetic interactions found between the Mn2*a* and Mn2*b* ions for the LT1 phase, however, the reader should be aware that those considerations also hold true without any restriction for the magnetic structure of the HT1 phase (for which Mn2*a* and Mn2*b* are further combined to a single magnetic site).

The detailed structural situation found between the adjacent Kagomé layers in the LT1 phase of lt-$Mn_3(VO_4)_2$ is depicted in Fig. 15a. At this point, the reader is reminded that for the HT1 phase, the bright and dark blue octahedra combine to a single site which is ferromagnetically aligned between the adjacent Kagomé layers. First we note that Mn1*a*/*b* cations of one Kagomé layer are not bridged *via* VO_4 tetrahedra to Mn1*a*/*b* cations of the adjacent layer. Therefore, the Mn1*a*/*b* ions are likely to play a subordinate role for this redox mediated exchange interaction, and we will only consider the Mn2*a*/*b* cations in the following discussion. This is further supported by considering the partial density of states as shown in Fig. 14a, which shows that the d-orbital energies of Mn2 lie closer to the empty d-states of vanadium than the d-orbitals of Mn1, especially when comparing the spin up with the spin down states. Regarding the magnetic structure reported in the previous section, it is also clear that only ferromagnetic superexchange interactions appear to be dominant for the Mn2 ions of the HT1 phase of two adjacent Kagomé layers as soon as ordering between the adjacent Kagomé layers arises (the splitting to Mn2*a* and Mn2*b* sites is only observed when reducing the temperature further below ~15 K). For the LT1 phase, it is furthermore worth noting that the vectors connecting the Mn2*a* (or alternatively Mn2*b*) ions with the oxygen ions of the vanadium tetrahedron form a nearly orthogonal coordinate system (arrows drawn in Fig. 15b) for the LT1 phase.

To find stereochemically reasonable orbital interaction pathways, it is important to consider the orientations of the different orbitals of Mn^{2+} and V^{5+}. For octahedral coordination, the low energy t_{2g} (d_{xy}, d_{yz}, d_{xz}) orbitals point towards the edges of the octahedron, whereas the high energy e_g (d_{z^2}, $d_{x^2-y^2}$) orbitals point towards the corners of the octahedron. For tetrahedrally coordinated vanadium, it is helpful to imagine a cube around the tetrahedron for the visualization of the orientation of the respective orbitals (see Fig. 15a and b). Within this cube, the high energy t_2 orbitals point towards the edges of the cube (different t_2 orbitals are indicated by the use of different colours for the edges in Fig. 15a and b), whereas the low energy e orbitals point towards the faces of the cube. One can now imagine two types of interaction pathways (indirect and direct), both of which can be used to explain the ferromagnetic alignment found between the Mn2*a* or the Mn2*b* ions.

– Indirect: superexchange could arise between the e_g orbitals of Mn2*a*/*b*, for which the electrons would have to be mediated *via* the p-orbitals of the oxygen ligands to be transferred to the t_2 orbitals of V^{5+} (see Fig. 16). From geometric considerations, one can easily see that the three different Mn2*a*/*b* ions connected to V^{5+} (see Fig. 15b) could transfer their electrons to different t_2 orbitals of V^{5+} (double/triple excited state) *via* the oxygen ions. This would give rise to ferromagnetic superexchange interactions in agreement with Hund's rule. For such a superexchange interaction to take

 This journal is © The Royal Society of Chemistry 2016

Open Access Article. Published on 03 November 2015. Downloaded on 8/26/2025 8:18:09 AM.
This article is licensed under a Creative Commons Attribution 3.0 Unported Licence.

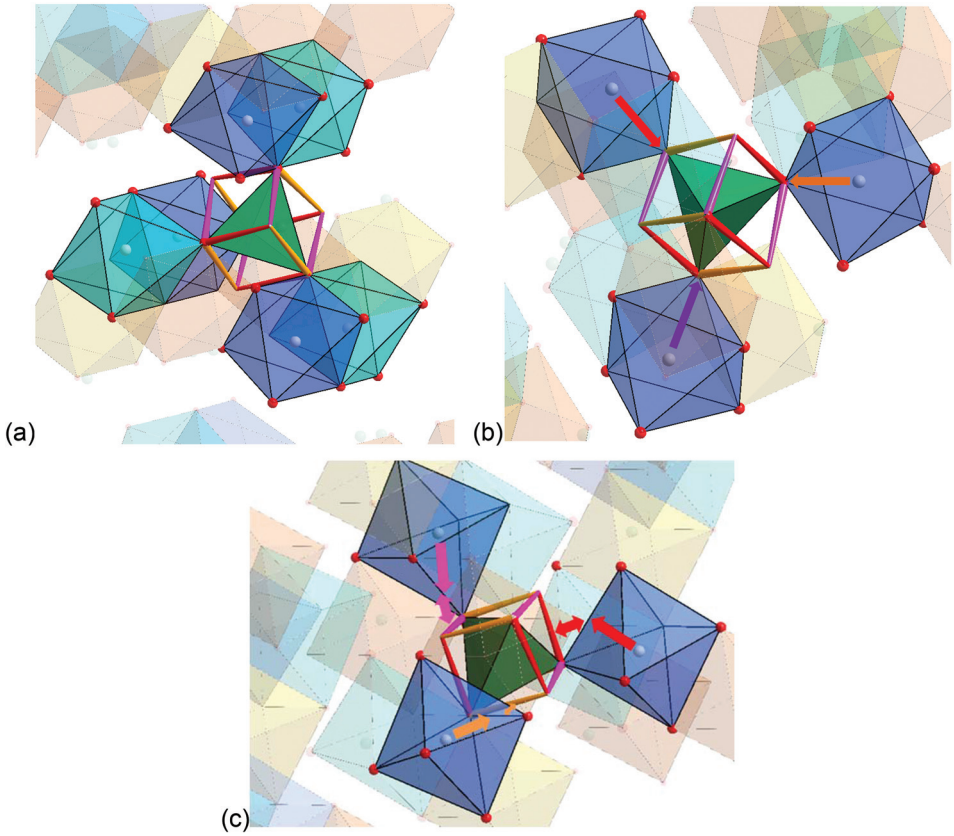

Fig. 15 (a) Structure excerpt of the LT1 phase of lt-$Mn_3(VO_4)_2$ to visualize the structural situation around the V^{5+} ion, which bridges adjacent Kagomé layers. A cube is drawn including the VO_4 tetrahedron to highlight the orientation of the d_{xy}, d_{yz}, and d_{xz} orbitals of V^{5+} (indicated by the red, purple, and orange edges of the cube). (b) Structure excerpt showing only the relative orientation of the Mn2*b* octahedra with respect to the bridging V^{5+} cation. Mn1*a* ions are located in the dark orange, Mn1*b* ions in the bright orange octahedra. Mn2*a* ions are located in the bright blue, Mn2*b* ions are located in the dark blue octahedra. For the HT1 phase of lt-$Mn_3(VO_4)_2$, both the light and dark blue octahedra would show ferromagnetic alignment of their magnetic moments. (c) Potential pathway for direct interactions between the t_{2g} orbitals of Mn^{2+} (indicated as coloured single tip arrows) with the t_2 orbitals of V^{5+} (indicated as coloured edges of the cube). Double tip arrows are used to indicate the proximity of the edges of the respective polyhedra.

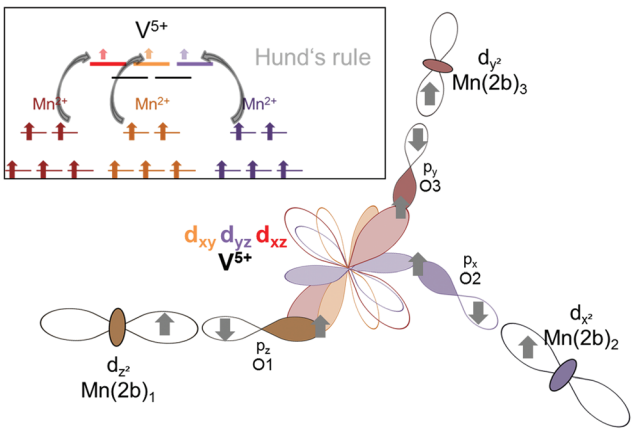

Fig. 16 Orbital interactions for redox-mediated M–M′(d^0-)–M superexchange expected in lt-$Mn_3(VO_4)_2$.

place it is important that the e_g orbitals of Mn^{2+} as well as the t_2 orbitals of V^{5+} as well as the p orbitals of O^{2-} do not differ too much in energy, and this assumption is well supported by our observations and DFT based calculations described above. We consider this to be the most likely interaction pathway for lt-$Mn_3(VO_4)_2$.

– Direct: additionally, one could also imagine a sort of direct interaction between the Mn^{2+} and the V^{5+} ions. Geometrically, this direct interaction cannot be mediated *via* the e_g orbitals of Mn^{2+}, since they are shielded by the oxide ions. Regarding the sketch shown in Fig. 15c, it can be seen that the edges of the octahedron (*i.e.* the place where the t_{2g} orbitals of Mn^{2+} point at) as well as the edges of the cube (*i.e.* the place where the t_2 orbitals of V^{5+} point at) are relatively close to each other (distances of the centres of the edges around 1.1 ± 0.07 Å). The Mn^{2+} shows an approximate distance of ~1.50 Å to the centre of the edge of the octahedron, and the distance of the V^{5+} ion to one edge of the cube is approximately 1.4 Å. This sums up to an interaction length of 4 Å, which seems quite large and most likely renders the direct pathway to a lower importance, but is only ~0.5 Å longer than the straight line connecting the Mn^{2+} and the V^{5+} ions *via* the O^{2-} anions. Apart from the considerations of the relative energy levels of

Open Access Article. Published on 03 November 2015. Downloaded on 8/26/2025 8:18:09 AM.
This article is licensed under a Creative Commons Attribution 3.0 Unported Licence.

the M^{2+} ions as discussed above, it is also evident that the strength of such a direct redox-mediated M–M′(d^0)–M superexchange would have to be different due to the different occupation of the t_{2g} levels of Mn^{2+}, Co^{2+}, and Ni^{2+} (see Fig. 11). Since the t_{2g} levels of Ni^{2+} are fully occupied, such a superexchange interaction would be basically forbidden, whereas for Co^{2+} it would be partially allowed. Since the other ligands of the MO_6 octahedra connect to different adjacent Kagomé layers, ferromagnetic interactions could not be mediated to both adjacent layers, and this might give an additional increment to the explanations of the incommensurability along *b* for $Co_3(VO_4)_2$ as given by Chen *et al.*[31]

4. Conclusions

We have shown that magnetic ordering of the low temperature modification of $Mn_3(VO_4)_2$ results in two magnetic phase transitions at low temperatures. On cooling below ~25 K, an antiferromagnetic order occurs between the magnetic moments on the Mn1 and Mn2 sites along the *a*-axis (HT1 phase, *Cmc′a′*), and this phase shows a high degree of spin frustration for the Mn2 site. Further cooling below ~17 K results in an ordering of the magnetic moments along the *b*-axis for the Mn2 ions, resulting in a release of spin frustration (LT1 phase, *Pmc′a′*). Short range ordering of magnetic moments along the *b*-plane can also be inferred for the HT1 phase. The magnetic structures reported here agree well with the findings of Morosan *et al.*[1] and Wang *et al.*[2] and provide new insights into the magnetic ordering of spin-frustrated systems with strong antiferromagnetic interactions within the Kagomé staircase structure. Peculiar differences in interlayer magnetic ordering compared to $Ni_3(VO_4)_2$ and $Co_3(VO_4)_2$ help to derive a ferromagnetic superexchange interaction, which seems to be the predominant superexchange pathway for $Mn_3(VO_4)_2$ and is promoted by V^{5+} with d^0 electronic configuration due to its energetic closeness to the Mn^{2+} d-levels as well as the distinct coordination geometry found for the Kagomé staircase structure.

Acknowledgements

The Institut Laue-Langevin is gratefully acknowledged for the allocation of beam time and technical support. O. Clemens wants to thank Prof. Dr H. P. Beck, Prof. Dr J. Manuel Perez-Mato, Prof. Dr K. Albe and Prof. Dr B. Albert for helpful discussion.

References

1 E. Morosan, J. Fleitman, T. Klimczuk and R. J. Cava, *Phys. Rev. B: Condens. Matter*, 2007, **76**, 144403.
2 X. Wang, Z. Liu, A. Ambrosini, A. Maignan, C. L. Stern, K. R. Poeppelmeier and V. P. Dravid, *Solid State Sci.*, 2000, **2**, 99–107.
3 G. M. Clark, R. Morley and A. N. Pick, *J. Inorg. Nucl. Chem.*, 1977, **39**, 1841–1843.
4 O. Clemens, R. Haberkorn and H. P. Beck, *J. Solid State Chem.*, 2011, **184**, 2640–2647.
5 O. Clemens, A. J. Wright, K. S. Knight and P. R. Slater, *Dalton Trans.*, 2013, **42**, 7894–7900.
6 O. Clemens, R. Haberkorn, M. Springborg and H. P. Beck, *J. Solid State Chem.*, 2012, **194**, 409–415.
7 M. Kenzelmann, A. B. Harris, A. Aharony, O. Entin-Wohlman, T. Yildirim, Q. Huang, S. Park, G. Lawes, C. Broholm, N. Rogado, R. J. Cava, K. H. Kim, G. Jorge and A. P. Ramirez, *Phys. Rev. B: Condens. Matter*, 2006, **74**, 014429.
8 P. L. Wang, P.-E. Werner and A. G. Nord, *Z. Kristallogr.*, 1992, **198**, 271–276.
9 A. G. Nord and P.-E. Werner, *Z. Kristallogr.*, 1991, **149**, 49–55.
10 E. E. Sauerbrei, R. Faggiani and C. Calvo, *Acta Crystallogr., Sect. B: Struct. Crystallogr. Cryst. Chem.*, 1973, **29**, 2304–2306.
11 H. Fuess, E. F. Bertaut, R. Pauthenet and A. Durif, *Acta Crystallogr., Sect. B: Struct. Crystallogr. Cryst. Chem.*, 1970, **26**, 2036–2046.
12 N. Qureshi, H. Fuess, H. Ehrenberg, T. C. Hansen, C. Ritter, K. Prokes, A. Podlesnyak and D. Schwabe, *Phys. Rev. B: Condens. Matter*, 2006, **74**, 212407.
13 G. Lawes, A. B. Harris, T. Kimura, N. Rogado, R. J. Cava, A. Aharony, O. Entin-Wohlman, T. Yildirim, M. Kenzelmann, C. Broholm and A. P. Ramirez, *Phys. Rev. Lett.*, 2005, **95**, 087205.
14 G. Lawes, M. Kenzelmann, N. Rogado, K. H. Kim, G. A. Jorge, R. J. Cava, A. Aharony, O. Entin-Wohlman, A. B. Harris, T. Yildirim, Q. Z. Huang, S. Park, C. Broholm and A. P. Ramirez, *Phys. Rev. Lett.*, 2004, **93**, 247201.
15 T. C. Hansen, P. F. Henry, H. E. Fischer, J. Torregrossa and P. Covert, *Meas. Sci. Technol.*, 2008, **19**, 034001.
16 E. Suard and A. Hewat, *Neutron News*, 2001, **12**, 30–33.
17 *Topas V4.2, General profile and structure analysis software for powder diffraction data, User's Manual*, Bruker AXS, Karlsruhe, Germany, 2008.
18 A. A. Coelho, TOPAS-Academic, http://www.topas-academic.net, accessed 20th of October 2014.
19 R. A. Young, *The Rietveld Method*, Oxford University Press, Oxford, 2002.
20 J. Enkovaara, C. Rostgaard, J. J. Mortensen, J. Chen, M. Dulak, L. Ferrighi, J. Gavnholt, C. Glinsvad, V. Haikola, H. A. Hansen, H. H. Kristoffersen, M. Kuisma, A. H. Larsen, L. Lehtovaara, M. Ljungberg, O. Lopez-Acevedo, P. G. Moses, J. Ojanen, T. Olsen, V. Petzold, N. A. Romero, J. Stausholm-Moller, M. Strange, G. A. Tritsaris, M. Vanin, M. Walter, B. Hammer, H. Hakkinen, G. K. Madsen, R. M. Nieminen, J. K. Norskov, M. Puska, T. T. Rantala, J. Schiotz, K. S. Thygesen and K. W. Jacobsen, *J. Phys.: Condens. Matter.*, 2010, **22**, 253202.
21 J. P. Perdew, K. Burke and M. Ernzerhof, *Phys. Rev. Lett.*, 1997, **78**, 1396.
22 J. P. Perdew, K. Burke and M. Ernzerhof, *Phys. Rev. Lett.*, 1996, **77**, 3865.

 This journal is © The Royal Society of Chemistry 2016

Open Access Article. Published on 03 November 2015. Downloaded on 8/26/2025 8:18:09 AM.
This article is licensed under a Creative Commons Attribution 3.0 Unported Licence.

23 A. I. Liechtenstein, V. I. Anisimov and J. Zaanen, *Phys. Rev. B: Condens. Matter*, 1995, **52**, R5467.
24 S. V. Gallego, E. S. Tasci, G. de la Flor, J. M. Perez-Mato and M. I. Aroyo, *J. Appl. Crystallogr.*, 2012, **45**, 1236–1247.
25 M. I. Aroyo, J. M. Perez-Mato, D. Orobengoa, E. Tasci, G. de la Flor and A. Kirov, *Bulg. Chem. Commun.*, 2011, **43**, 183–197.
26 M. I. Aroyo, J. M. Perez-Mato, C. Capillas, E. Kroumova, S. Ivantchev, G. Madariaga, A. Kirov and H. Wondratschek, *Z. Kristallogr.*, 2006, **221**, 15–27.
27 M. I. Aroyo, A. Kirov, C. Capillas, J. M. Perez-Mato and H. Wondratschek, *Acta Crystallogr., Sect. A: Fundam. Crystallogr.*, 2006, **A62**, 115–128.
28 MAXMAGN in the Bilbao Crystallographic Server, http://cryst.ehu.es, accessed 20th of October 2014.
29 MGENPOS in the Bilbao Crystallographic Server, http://cryst.ehu.es, accessed 20th of October 2014.
30 W. Hamilton, *Acta Crystallogr.*, 1965, **18**, 502–510.
31 Y. Chen, J. W. Lynn, Q. Huang, F. M. Woodward, T. Yildirim, G. Lawes, A. P. Ramirez, N. Rogado, R. J. Cava, A. Aharony, O. Entin-Wohlman and A. B. Harris, *Phys. Rev. B: Condens. Matter*, 2006, **74**, 014430.
32 T. Degen, M. Sadki, E. Bron, U. König and G. Nénert, *Powder Diffr.*, 2014, **29**, S13–S18.
33 R. Toft-Petersen, N. H. Andersen, H. Li, J. Li, W. Tian, S. L. Bud'ko, T. B. S. Jensen, C. Niedermayer, M. Laver, O. Zaharko, J. W. Lynn and D. Vaknin, *Phys. Rev. B: Condens. Matter*, 2012, **85**, 224415.
34 G. Lautenschläger, H. Weitzel, T. Vogt, R. Hock, A. Böhm, M. Bonnet and H. Fuess, *Phys. Rev. B: Condens. Matter*, 1993, **48**, 6087–6098.
35 A. Authier, *International Tables for Crystallography Volume D: Physical Properties of Crystals*, Kluwer Academic Publishers, Dordrecht/Boston/London, 2013.
36 J. B. Goodenough, *Magnetism and the Chemical Bond*, Interscience Publisher, New York, 1963.
37 J. B. Goodenough, *Phys. Rev.*, 1960, **117**, 1442–1451.
38 A. K. Bera, B. Lake, W. D. Stein and S. Zander, *Phys. Rev. B: Condens. Matter*, 2014, **89**, 094402.
39 H.-J. Koo and M.-H. Whangbo, *Inorg. Chem.*, 2006, **45**, 4440–4447.
40 K. Ghoshray, B. Pahari, B. Bandyopadhyay, R. Sarkar and A. Ghoshray, *Phys. Rev. B: Condens. Matter*, 2005, **71**, 214401.
41 H. B. Yahia, E. Gaudin, C. Lee, M. H. Whangbo and J. Darriet, *Chem. Mater.*, 2007, **19**, 5563–5569.
42 O. Clemens, R. Haberkorn, H. Kohlmann, M. Springborg and H. P. Beck, *Z. Anorg. Allg. Chem.*, 2012, **638**, 1134–1140.
43 O. Clemens, Ph.D. Dissertation, Universität des Saarlandes, 2011.
44 O. Clemens, M. Bauer, R. Haberkorn and H. P. Beck, *Z. Anorg. Allg. Chem.*, 2011, **637**, 1036–1044.
45 O. Clemens, R. Haberkorn, M. Springborg and H. P. Beck, *Z. Anorg. Allg. Chem.*, 2014, **640**, 173–183.
46 A. K. Padhi, K. S. Nanjundaswamy and J. B. Goodenough, *J. Electrochem. Soc.*, 1997, **144**, 1188–1194.
47 O. Clemens, M. Bauer, R. Haberkorn, M. Springborg and H. P. Beck, *Chem. Mater.*, 2012, **24**, 4717–4724.
48 F. Zhou, M. Cococcioni, K. Kang and G. Ceder, *Electrochem. Commun.*, 2004, **6**, 1144–1148.
49 F. Zhou, M. Cococcioni, C. A. Marianetti, D. Morgan and G. Ceder, *Phys. Rev. B: Condens. Matter*, 2004, **70**, 235121.
50 L. L. Y. Chang and F. Y. Wang, *J. Am. Ceram. Soc.*, 1988, **71**, 689–693.